Journal of Volcanology and Geothermal Research 391 (2020) 106337

Contents lists available at ScienceDirect

Journal of Volcanology and Geothermal Research

journal homepage: www.elsevier.com/locate/jvolgeores

Injection-induced surface deformation and seismicity at the Hellisheidi geothermal field, Iceland

D. Juncu[a,*], Th. Árnadóttir[a], H. Geirsson[a], G.B. Guðmundsson[b], B. Lund[c], G. Gunnarsson[d], A. Hooper[e], S. Hreinsdóttir[f], K. Michalczewska[a]

[a] Nordic Volcanological Center, Institute of Earth Sciences, University of Iceland, Reykjavik, Iceland
[b] Icelandic Meteorological Office, Reykjavik, Iceland
[c] Department of Earth Sciences, Uppsala University, Uppsala, Sweden
[d] OR–Reykjavik Energy, Reykjavik, Iceland
[e] COMET, School of Earth and Environment, University of Leeds, Leeds, UK
[f] GNS Science, Lower Hutt, New Zealand

ARTICLE INFO

Article history:
Received 30 June 2017
Received in revised form 22 January 2018
Accepted 21 March 2018
Available online 5 April 2018

Keywords:
Man-made deformation
Induced seismicity
Fluid injection
Geodesy
Geothermal energy

ABSTRACT

Induced seismicity is often associated with fluid injection but only rarely linked to surface deformation. At the Hellisheidi geothermal power plant in south-west Iceland we observe up to 2 cm of surface displacements during 2011–2012, indicating expansion of the crust. The displacements occurred at the same time as a strong increase in seismicity was detected and coincide with the initial phase of geothermal wastewater reinjection at Hellisheidi. Reinjection started on September 1, 2011 with a flow rate of around 500 kg/s. Micro-seismicity increased immediately in the area north of the injection sites, with the largest seismic events in the sequence being two M4 earthquakes on October 15, 2011. Semi-continuous GPS sites installed on October 15 and 17, and on November 2, 2011 reveal a transient signal which indicates that most of the deformation occurred in the first months after the start of the injection. The surface deformation is evident in ascending TerraSAR-X data covering June 2011 to May 2012 as well. We use an inverse modeling approach and simulate both the InSAR and GPS data to find the most plausible cause of the deformation signal, investigating how surface deformation, seismicity and fluid injection may be connected to each other. We argue that fluid injection caused an increase in pore pressure which resulted in increased seismicity and fault slip. Both pore pressure increase and fault slip contribute to the surface deformation.

1. Introduction

Fluid induced seismicity is of great concern because it poses a risk to safety, infrastructure and acceptance of energy production operations. It can either be caused directly by changes in pore pressure due to injection or extraction of fluids, or by stress changes that are induced by the injection or extraction (see Ellsworth, 2013; Zang et al., 2014; Segall and Lu, 2015). Causes of induced earthquakes include injection of fluids (e.g. Healy et al., 1968; Majer and Peterson, 2007; Rutqvist and Oldenburg, 2008; Evans et al., 2012), formation of water reservoirs for hydroelectricity generation (e.g. Chopra and Chakrabarti, 1973), secondary recovery of hydrocarbons (e.g. Davis and Pennington, 1989) and production of hydrocarbons (Segall, 1989). Injection of fluids at geothermal sites has caused seismic activity, as described by, e.g., Deichmann and Giardini (2009) and Dorbath et al. (2009). Flóvenz et al. (2015) give an overview of examples of injection related seismicity at geothermal fields in Iceland. At the Hellisheidi geothermal field in SW Iceland, seismic swarms have been observed at the injection site at Húsmúli starting with the drilling and testing of boreholes and continuing during injection (see e.g. Flóvenz et al., 2015; Gunnarsson et al., 2015).

Finding a connection between induced seismicity and fluid injection is important to improve our understanding of the generation of fluid driven seismicity. Surface deformation can provide evidence of pore pressure increase caused by wastewater injection, which in turn can cause induced seismicity. Only a few studies report measurements of injection-induced surface deformation linked to seismicity. Such observations have been described by, e.g., Ottemöller et al. (2005) at

* Corresponding author.
E-mail address: daj22@hi.is (D. Juncu).

https://doi.org/10.1016/j.jvolgeores.2018.03.019

the Ekofisk oil field in the North Sea, Jahr et al. (2008) at a large-scale injection experiment in south-east Germany and Shirzaei et al. (2016) at an injection site for disposals from oil and gas production in Texas, USA. Fialko and Simons (2000) reported injection related deformation and seismicity at the geothermal site Coso, California, USA. All these studies indicate pore pressure changes as a possible cause (or one of the causes) for the induced seismicity.

In this study, we present data describing an episode of simultaneous surface deformation and seismicity at the Hellisheidi high temperature geothermal field in SW Iceland (Fig. 1). The field is located within the Hengill Volcanic System which last erupted around 2000 years BP. The most recent unrest episode took place between 1993 and 1998, with an increase in earthquake activity in combination with surface uplift (Sigmundsson et al., 1997; Feigl et al., 2000; Clifton et al., 2002). Seismic activity peaked in June and November 1998 with two earthquakes of magnitude M_W 5.4 and 5.1, respectively (Vogfjörd and Slunga, 2003; Jakobsdóttir, 2008). Hengill is at the junction of three segments of the boundary between the North American, Eurasian and Hreppar micro-plate. These segments are the obliquely spreading Reykjanes Peninsula (RP) to the southwest, the Western Volcanic Zone (WVZ) to the north and the ~100 km long, transform-type South Iceland Seismic Zone (SISZ) to the east (Fig. 1). In the SISZ, earthquake sequences recur at average intervals of 80–120 years on faults that are predominantly strike-slip with N–S orientation, typical of bookshelf tectonics (Stefánsson and Halldórsson, 1988; Einarsson, 1991). The most recent events of the current sequence occurred in June 2000 with two M_W 6.5 earthquakes (Árnadóttir et al., 2001; Pedersen et al., 2003) and in May 2008 with two M_W 6 earthquakes (Hreinsdóttir et al., 2009; Decriem et al., 2010). The 2008 earthquakes were located approximately 15 km east of the study area at Húsmúli. Both the 2000 and the 2008 events triggered micro-earthquakes in the Hengill area.

Geothermal power production at the Hellisheidi field started in 2006 with an extraction rate of 7 Mton/yr which had been increased to 30 Mton/yr by 2011 (Gunnlaugsson, 2016). A consistent decrease in reservoir pressure of 0.2–0.3 MPa/yr has been observed since 2007 (Haraldsdóttir, 2014). The pressure change causes local surface subsidence; up to ~2 cm/yr between 2012 and 2015 (Juncu et al., 2017). In order to maintain pressure in the reservoir, wastewater reinjection was started in 2007 at the Gráhnúkar site (Fig. 1). The second injection site, Húsmúli, was commissioned on 1 September 2011 with an initial flow rate of around 500 kg/s (Gunnarsson, 2013b). After the injection started, increased earthquake activity was observed in the Húsmúli area. The largest events after the beginning of the injection were of magnitude 4 and occurred on 15 October 2011 (Bessason et al., 2012, see locations on Fig. 1). They were widely felt in the capital area 20 km to the west. Immediately following the M4 events in October, four Global Positioning System (GPS) benchmarks in the vicinity of Húsmúli were observed semi-continuously for several months to monitor surface deformation (Fig. 1). In this study, we will use the so collected GPS data jointly

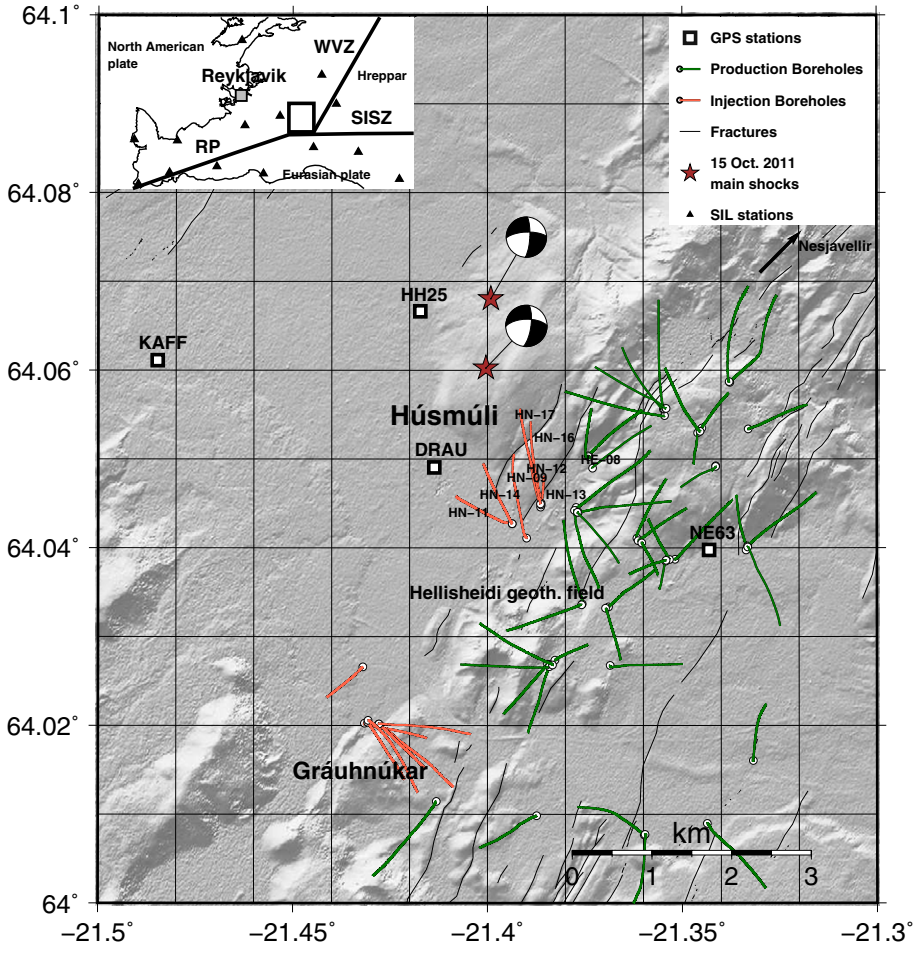

Fig. 1. The Hellisheidi geothermal field and the Húsmúli reinjection zone. White squares denote GPS benchmarks used in this study, black lines show mapped surface fractures (Clifton et al., 2002; Einarsson, 2008), green and red lines show trajectories of production and injection boreholes, respectively. The red stars show the location of the 15 October 2011 main shocks, the beach ball plots show their respective focal mechanisms. Seismic stations of the SIL network are shown as black triangles in the insert on the top left. The plate boundary segments are marked as black lines. The segments are: the Reykjanes peninsula (RP), the Western Volcanic Zone (WVZ) and the South Iceland Seismic Zone (SISZ).

with Interferometric Synthetic Aperture Radar (InSAR) data to measure deformation. We analyze and model the GPS and InSAR data to investigate how the fluid injection at Hellisheidi relates to surface deformation and how the deformation is linked to the seismicity.

2. Seismicity & fluid injection

Seismicity in Iceland is continuously monitored by the national seismic network of Iceland, the SIL network, which has been in operation since 1991 (Böðvarsson et al., 1996, 1999). During 2011 and 2012, twelve seismic stations were located within 50 km of the injection site of which five were within 25 km (Fig. 1). The closest SIL seismic station is about 8 km to the west of the injection boreholes. Four of these twelve stations have Lennartz LE-3D/1s sensors, the other eight have Lennartz LE-3D/5s sensors. Most of the stations are equipped with a RD3 digitizer from Nanometrics, the others have a Guralp digitizer. The sampling rate for all stations is 100 Hz. The SIL system automatically detects and locates earthquakes which are then manually quality controlled. The automatic system determines single event locations using the SIL 1D velocity model (Stefánsson et al., 1993). A multi-event double-difference relocation method is available in the system (Slunga et al., 1995). We estimate multi-event locations using a local velocity model for the SISZ (Vogfjörd et al., 2002). Focal mechanisms are calculated for all manually processed events using a spectral amplitude methodology which estimates the double-couple part of the moment tensor (Slunga, 1981; Rögnvaldsson and Slunga, 1993, 1994).

The Húsmúli area first showed signs of induced seismicity with magnitudes up to ~M2 during the drilling of the production well HE-08 in 2002, and again during drilling and testing of the injection wells HN-12 in 2009 and HN-17 in February 2011 (Fig. 1; Björnsson, 2004; Bessason et al., 2012; Gunnarsson, 2013b; Ágústsson et al., 2015). In contrast, the injection at Gráhnúkar (Fig. 1), which began in 2007 and had an average injection rate of 170 kg/s in 2011, only caused very little micro-seismicity(Gunnarsson, 2013b; Ágústsson et al., 2015). Injection at Húsmúli started 1 September 2011, with the rate being increased over several days until it reached 480 kg/s on 8 September (Fig. 2). Initially, the flow rate was distributed over four boreholes, HN-09, HN-12, HN-14 and HN-17 (Figs. 1 & 3). Injection into a fifth borehole, HN-16, began on 23 September. The excess injection pressure was approximately 2.8 MPa (Gunnarsson, 2013a). Pressure increase was observed in nearby boreholes; 0.14 MPa between October 2011 and April 2012 in HN-13 (Gunnarsson, 2013a), and 0.08 MPa between September and November 2011 in HE-08 (Gunnarsson, 2012). Micro-seismicity started to increase around 10 September 2011 (Fig. 2), beginning around and north of HN-12 and HN-17 as well as close to HN-14 (Fig. 3a). In the following days the activity spread further north of HN-12 and HN-17. Until 16 September this was the main area of activity, highlighting a NNE-SSW striking feature of around 2 km length (see Fig. 3b). On 17 September, the seismicity spread westward to the area north of HN-14 (Fig. 3c). In the following weeks, activity continued in both areas, outlining a second N–S zone parallel to the eastern line of activity (Fig. 3d). Two mainshocks occurred on 15 October north of HN-14 within 40 min of each other, with local magnitudes of M4 (Fig. 3e). For the following three months, activity was mainly focused on the eastern and central zones (Fig. 3f). In mid-January 2012, the activity shifted approximately 1 km further westwards towards a third structure, south of the GPS station HH25 (Fig. 1). This was the main zone of seismic activity until May 2012 (Fig. 3g).

The focal mechanisms of the earthquakes, including the two largest events, indicate primarily right-lateral strike-slip with a small component of normal faulting (Fig. 1), on steeply eastward dipping faults. The first of the two M4 events has a strike of 8°, dip of 72° and rake of −152°; the second one has a strike 3°, dip of 76° and rake of −159°. The injection rate has been fairly constant with yearly averages between 380 and 450 kg/s during 2012–2015 (Gunnlaugsson, 2016). Recurrent episodes of increased seismicity have been observed during the same time interval.

3. Geodetic data

3.1. GPS

Following the M4 earthquakes on 15 October 2011, four GPS campaign benchmarks in the vicinity of Húsmúli were occupied semi-continuously (continuous deployment but manual data download) for several months. Measurements started on October 15 at DRAU

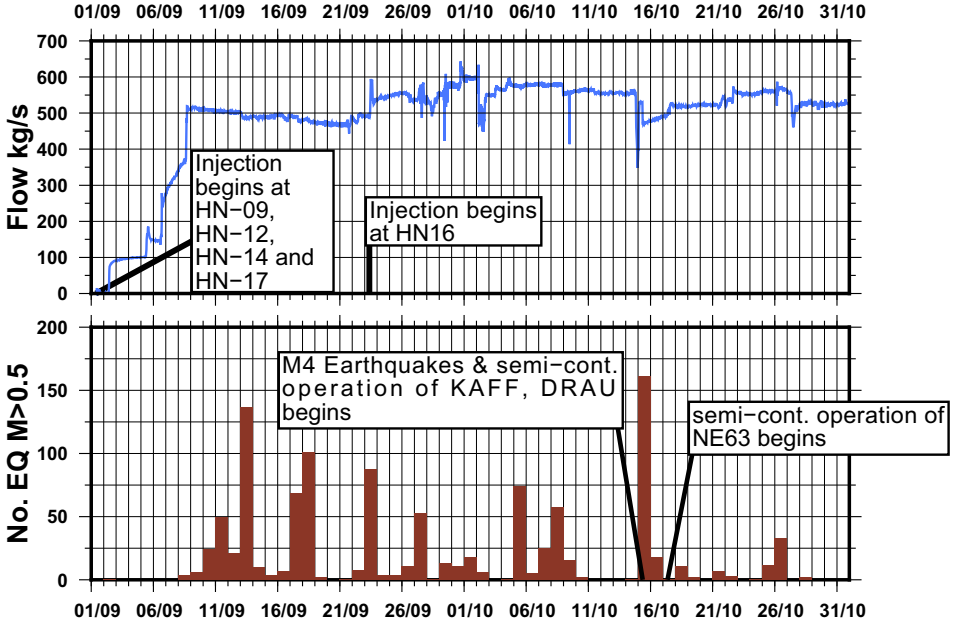

Fig. 2. Injection flow rate (top) and daily number of earthquakes (bottom) during September and October 2011 (Bessason et al., 2012). The timeline begins with the start of the injection on September 1, 2011.

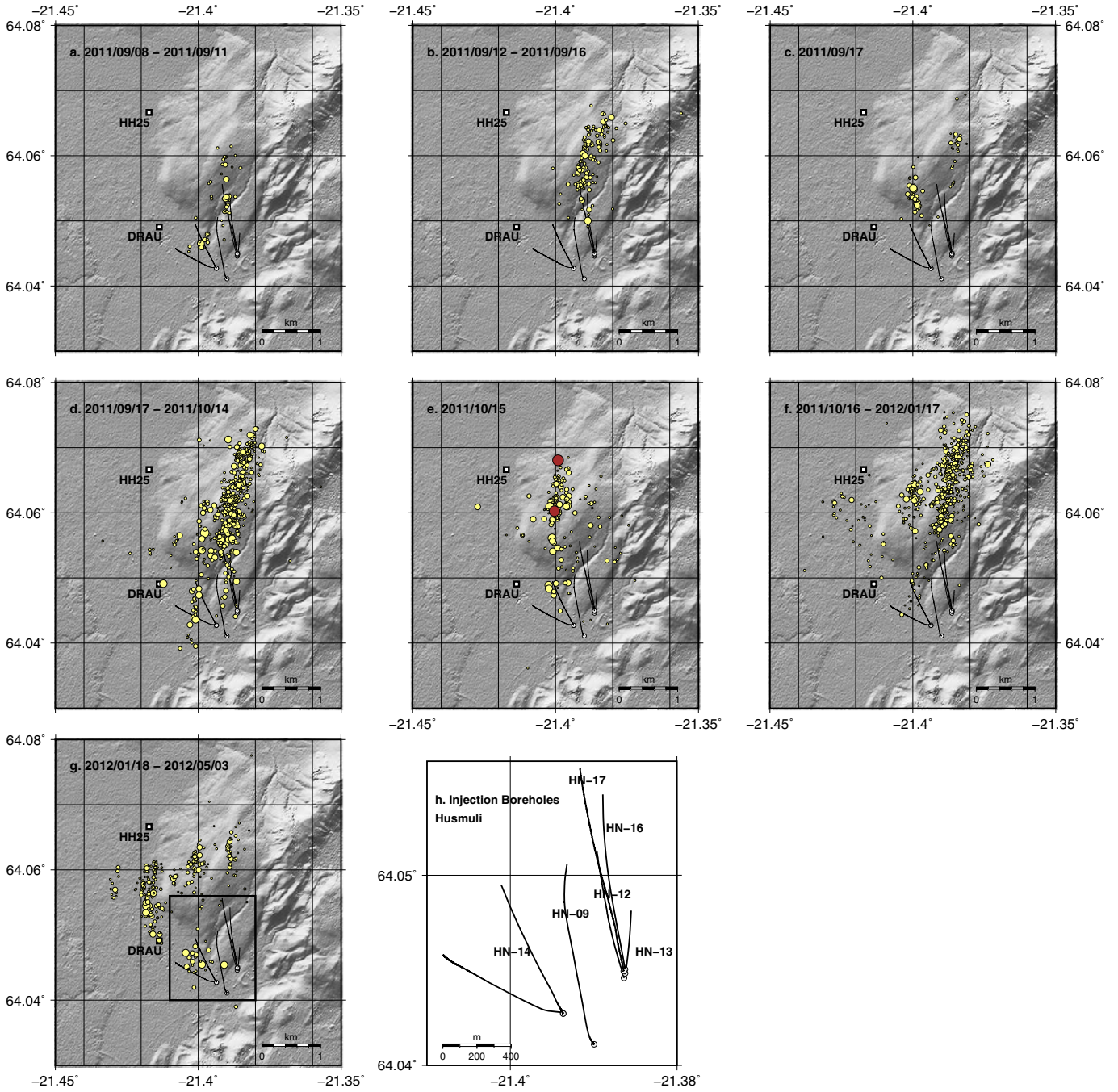

Fig. 3. Earthquakes in the vicinity of the reinjection site at Húsmúli (a–g), positions of the small events (yellow circles) are relative relocations. Red circles are M4 main shocks (single event locations), white squares are GPS site locations, labeled with four letter acronyms. Plot h shows borehole locations and names for the injection boreholes within the area outlined with a black rectangle in plot g. The circles indicate the locations of wellheads and the lines show the surface projection of the holes. Borehole depths are between 1.9 km and 3 km.

and KAFF, on October 17 at NE63 and on November 2 at HH25 (see Figs. 1 and 2). The data were analyzed with the GAMIT software, version 10.6 (Herring et al., 2015). Continuous GPS stations in Iceland and over 100 global reference stations were included to determine the daily solutions in the ITRF08 reference frame (Altamimi et al., 2012). To estimate GPS station positions we used the GLOBK software, version 5.29 (Herring et al., 2015).

We use the GPS time series to discern between constant background velocity—consisting of plate motion relative to the reference frame and assumed steady state deformation field—and the transient that started with the injection at Húsmúli (Supplement 1). We calculate the background velocities using pre-transient data to detrend the GPS time-series (Fig. 4) and estimate the total transient displacements until mid-2012 to employ them in the joint inversion (Section 4.1). The stations west and northwest of the injection area (HH25, DRAU, KAFF) show a net westward and/or northward motion, whereas NE63, located in the southeast, shows motion to the southeast. We do not include the vertical GPS displacements in this study because we have good constraints on vertical motion from the InSAR data.

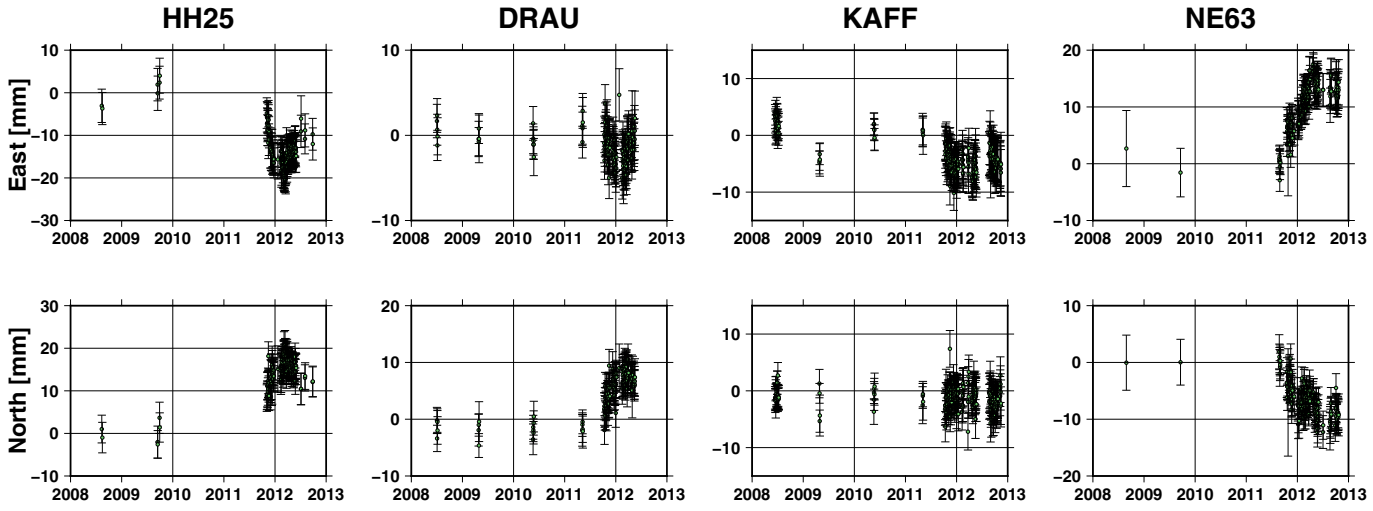

Fig. 4. Position time series 2008-2013 of the GPS stations HH25, DRAU, KAFF and NE63. The ITRF08 time series were detrended using the pre-transient velocities (see Supplement 1).

3.2. InSAR

We use satellite-borne synthetic aperture radar (SAR) data, obtained by the TerraSAR-X mission of the German aerospace center (Table 1), in addition to the GPS data to measure surface deformation. Using interferometry (interferometric SAR: InSAR), the SAR acquisitions are processed to obtain relative ground displacements in the line of sight (LOS) of the satellite (see, e.g., Dzurisin, 2007).

We create interferograms with the DORIS software (Kampes et al., 2003) and use the 25 m resolution intermediate TanDEM-X digital elevation model (DEM) to account for topographic contributions to the measured signal. Even though we are only interested in a short time interval covering September 2011 until mid-2012, which is covered by a single interferogram, we use a multitemporal InSAR approach (Hooper, 2008) for which we use the StaMPS software (Hooper et al., 2012). The multitemporal approach is useful because it results in increased signal-to-noise ratio for the single interferogram that we use. We use a set of 35 interferometric pairs spanning 2009–2015 from TerraSAR-X track 41 to find the pixels that decorrelate little over short time intervals (Hooper, 2008). On the interferograms we suspect to be affected by atmospheric noise we apply a linear phase-correction for tropospheric delay which is based on topography (Bekaert et al., 2015b). We choose an interferogram spanning 30 June 2011 to 03 May 2012 (Fig. 5) because of the interferograms that cover the first months after the injection at Húsmúli started, it has the strongest signal-to-noise ratio and shows the least signs of decorrelation. The satellite takes images at close to 30° from the vertical (Table 1) and the average LOS unit vector for the imaged area is [−0.50, −0.12, 0.86] (east, north, up), which means that the measurements are mainly sensitive to vertical and E-W motion. We estimate the full variance-covariance matrix for the spatially correlated InSAR data following the method of Bekaert et al. (2015a). We obtain a variance of $\sigma^2 = 28.8\,\mathrm{mm}^2$, a range of 16.5 km and a nugget term of 0.05 mm^2, which we use to calculate the exponential covariance function. Residual topographic signal and orbit errors are estimated and subtracted during the StaMPS workflow. We assume that any remaining contributions from these sources are taken into account by our approach for estimating the variance-covariance matrix.

To isolate the local signal, we correct the interferogram for plate motion as well as anthropogenic deformation related to the geothermal energy production at the Hengill power plants (i.e., the Hellisheidi and Nesjavellir production areas), using results from Árnadóttir et al. (2009) and Juncu et al. (2017). The most prominent signal that remains is motion of over 20 mm towards the satellite (i.e., mostly upwards and/or westwards) in the Húsmúli area (Fig. 5). Because the data have strong spatial correlation, we can downsample them without losing significant information, using a pixel-variance–based quadtree algorithm (Jónsson et al., 2002, see Fig. 5).

Table 1
Satellite and orbit configuration of TerraSAR-X track 41.

TerraSAR-X T41	Configuration
Mode	StripMap
Heading	346.5° (ascending)
Look direction	Right
Look Angle	27.2°–29.5°
Altitude	515 km
Latitude	64.05°
Wavelength	31 mm (X-band)
Resolution	3 m
Covered area	50 km × 30 km

4. Modeling

4.1. Inverse deformation modeling

We test different elastic half-space models to relate subsurface processes to surface deformation: an opening or slipping rectangular dislocation (Okada, 1985), a spherical pressure source (McTigue, 1987) or a pressurized circular crack (Fialko et al., 2001). In all of our models, we fix the rheological parameters to a shear modulus of $\mu = 10\,\mathrm{GPa}$ and Poisson's ratio of $\nu = 0.25$, following other studies of deformation in geothermal areas (see Fialko and Simons, 2000; Keiding et al., 2010; Juncu et al., 2017).

We use a nonlinear Bayesian optimization method, CATMIP (Minson et al., 2013), to obtain the model parameters that optimize the fit to the surface deformation. The algorithm uses the annealing method (see Kirkpatrick et al., 1983) and runs multiple Markov chains (e.g. Gelman et al., 2014) to explore the parameter space. This way, it samples the posterior probability density function of the parameter space which is proportional to the product of the likelihood of a tested solution and the prior probability density function of

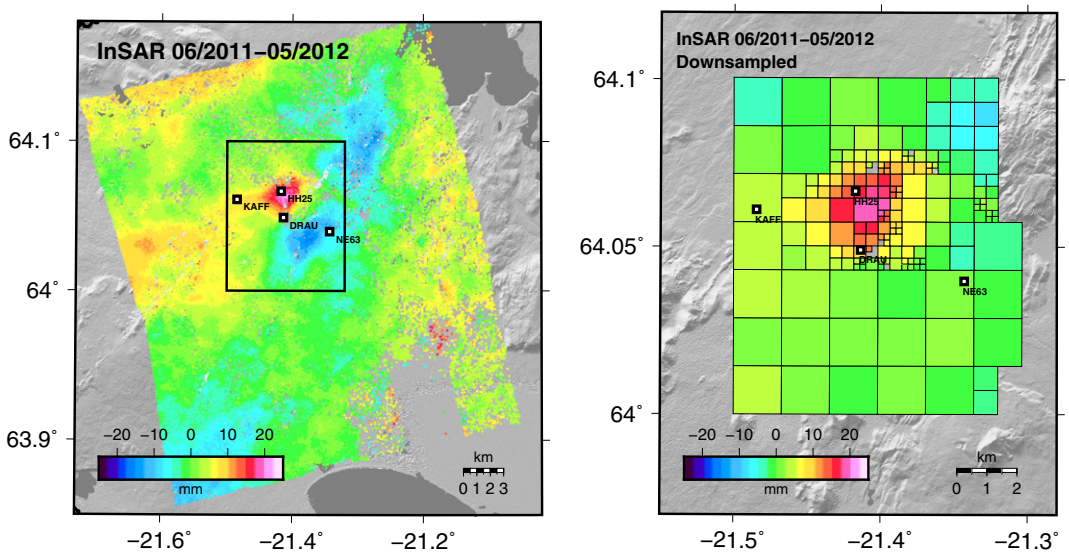

Fig. 5. Left: TerraSAR-X interferogram showing Line of Sight (LOS) motion in mm observed from the satellite between 30.06.2011and 03.05.2012. Negative values represent motion of the ground away from the satellite, positive values represent motion towards the satellite. Reference value is the mean value of the whole area. The black rectangle contains the data that are downsampled for the right-hand plot. Right: Cropped and downsampled data after being corrected for plate motion, subsidence related to magmatic activity and extraction of geothermal fluids (Árnadóttir et al., 2009; Juncu et al., 2017). The corrected interferogram before downsampling is shown in Supplement 3.

its parameters. The likelihood function $p(\mathbf{D}|\boldsymbol{\theta})$ allows us to calculate the probability of the observed data $\mathbf{D}$ given a model $\boldsymbol{\theta}$,

$$p(\mathbf{D}|\boldsymbol{\theta}) = \frac{1}{(2\pi)^{N_{dp}/2}|\mathbf{C}|^{\frac{1}{2}}} e^{-\frac{1}{2}\chi^2}, \quad (1)$$

where $\chi^2 = \mathbf{r}^T\mathbf{C}^{-1}\mathbf{r}$. Here, $\mathbf{r}$ is the residual between observed and model data points ($r = d_{obs} - d_{calc}$), $\mathbf{C}$ the data covariance matrix, N_{dp} the number of data points and T is the matrix transpose.

We perform a joint optimization for both GPS and InSAR data. In case of the InSAR data, $\mathbf{C}$ is the full variance-covariance matrix based on spatial correlation between data points (Section 3.2). For the GPS data only the main diagonal of $\mathbf{C}$ is non-zero, containing the variance values of the GPS data and assuming no spatial correlation between data points. The standard deviation of the InSAR data is 5.4 mm (see Section 3.2) and between 2.5 and 3.5 mm for the GPS data (see Supplement 1). We do not apply relative weights between the two datasets.

4.2. Results

Our main interest in this study is to identify the process that causes the observed surface deformation and whether we can connect it to the intense seismic activity. To this end, we run a joint optimization (see above) using the local total displacements that occurred during the transient.

The non-uniqueness of the optimization problem, as well as the many different physical processes that may have caused the observed deformation, make it difficult to select a single optimal solution. We test a variety of elastic half-space models and find several models that fit the data well (see below and Supplement 2). We use additional qualitative constraints to discern whether these models are feasible and how they compare against each other. We present two models (A and B) that we suggest to be the most realistic. Both of them are in agreement with the observations but they have different physical meaning.

4.2.1. Model A: single source

Model A is a rectangular dislocation for which we only allow opening motion and solve for its location, size, dip and strike (8 free parameters in total). The optimal solution is a roughly 2 by 1 km opening dislocation, dipping 80° towards northwest, opening by 40 cm with a depth to the top of the structure of 1.7 km (see Fig. 6, as well as Table 2 for parameter values and confidence intervals). The chi-squared value of the fit is $\chi^2 = 205$, implying 28% variance reduction (null-model: $\chi^2_{nm} = 285$).

The most notable misfit is the northward motion of DRAU. Also, Model A predicts negative LOS motion around the injection-wellheads which is not seen in the data. We show predicted LOS displacements for Model A for the full InSAR dataset in Supplement 3.

4.2.2. Model B: two sources

Model B combines a spherical pressure source and a right-lateral strike-slip fault. We fix the fault orientation to have a strike of 5° and a dip towards east, in agreement with the majority of the focal mechanisms. The results are shown in Fig. 7 and Table 3. This model has 13 free parameters and gives a variance reduction of 45%. The spherical pressure source is located at 2.7 km depth (90% confidence interval, CI, ranging from 2.3 to 3.0 km), with a radius of 1.1 km (90% CI: 0.8 to 1.4 km). The center of the sphere is located around 500 m north of the injection sites. The fault has mainly a right-lateral strike-slip component of 45 cm, and minor dip-slip (normal) of 4 cm. It dips 84° to the east and the slip is concentrated between 0.7 km and 1.1 km depth.

Unlike Model A, Model B reproduces the northward motion of DRAU (Fig. 7). The positive LOS motion around and south of the injection site, however, can not be seen in the data. This can also be seen when we plot the results for Model B for the full InSAR dataset, as shown in Supplement 3.

5. Discussion

5.1. Causes of deformation

We observe a transient deformation signal in the area around the Húsmúli injection site (Figs. 4 & 5) and investigate how deformation and injection may be linked. The transient starts with the

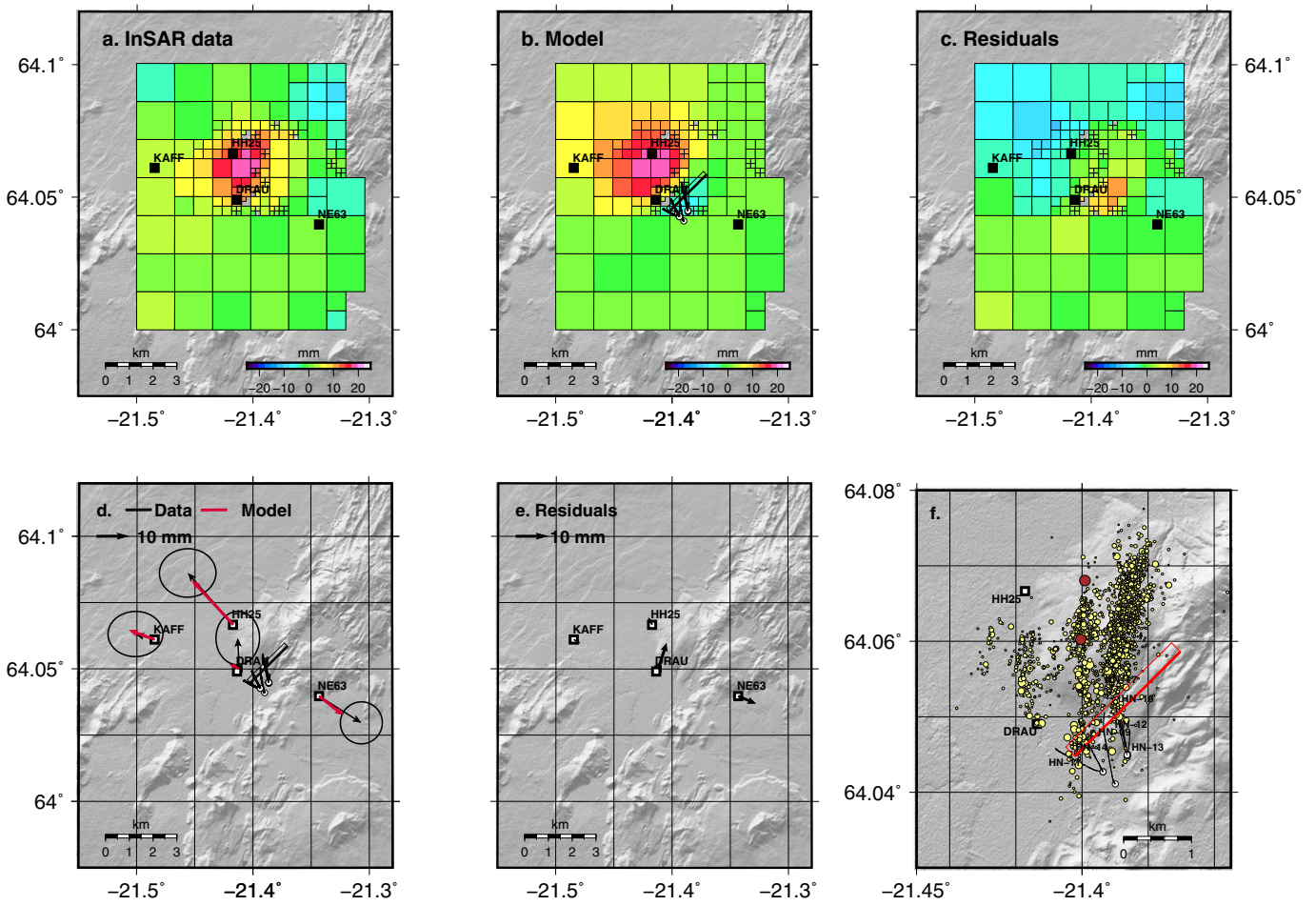

Fig. 6. Model A: InSAR data (a), model (b) and residuals (c) in the top row. All in LOS of the satellite. GPS data and model (d), residuals (e), as well as the location of the rectangular dislocation relative to the seismicity and the locations of the injection boreholes (f) in the bottom row. The rectangle marks the dislocation, the bold line representing the upper edge.

injection in September 2011 and has a peak in total deformation around February/March 2012, before reversing partly and stopping mid-2012 (Fig. 4). The spatial deformation pattern during this time interval indicates that part of the deformation stems from an expansive source, because surface displacements are pointing away from the injection site (Figs. 6 & 7). We test several subsurface processes that could be responsible for the observed surface displacements:

- expansion of a fracture or layer, caused by local increase in fluid pressure in the vicinity of the injection site (Model A)
- pressure increase in a wider area surrounding the injection site (Model B)
- fault slip (Model B)

In the previous section, we presented the models A and B that simulate one or more of these processes and are able to explain the surface deformation at Húsmúli occurring between the beginning of the injection in September 2011 and mid-2012. The combination of spatially dense InSAR data, which are most sensitive to vertical motion, and horizontal GPS data gives us good constraints on the location and the strength of the deformation source(s). However, the deformation signal is small, making it difficult to distinguish between different source types. These models represent different physical processes, both as the cause of deformation and how they may relate to micro-seismicity. We therefore consider qualitatively how the deformation sources could have contributed to the observed induced micro-seismicity and use this to select a preferred model. If a model indicates pore pressure increase around the earthquake foci (model B), the increase of pore pressure can be seen as a direct cause of the seismicity by reducing the effective normal stress on the seismogenic faults. If there is no pressure increase around the foci (model A, if we ignore pore pressure increase due to rock compression), the two most likely possibilities are, (a) the pressure increase does not cause detectable surface deformation but is still a possible cause for the seismicity or, (b) the seismicity is caused by an increase in Coulomb failure stress.

Table 2
Parameters and 90% confidence intervals for model A after joint inversion of GPS and InSAR data. The shear modulus we use is $\mu = 10$ GPa and Poisson's ratio is $\nu = 0.25$.

Model A		
Free model parameters		8
No. of data		179
χ^2		205
Dislocation		**90% CI**
Longitude [° W]	21.386	(21.371; 21.394)
Latitude [° N]	64.052	(64.045; 64.057)
Length [km]	2.2	(1.2; 4.4)
Width [km]	1.1	(0.2; 2.7)
Depth to top [km]	1.7	(1.0; 2.4)
Dip [°]	80	(63; 90)
Strike [°]	45	(30; 60)
Opening [m]	0.39	(0.11; 0.78)

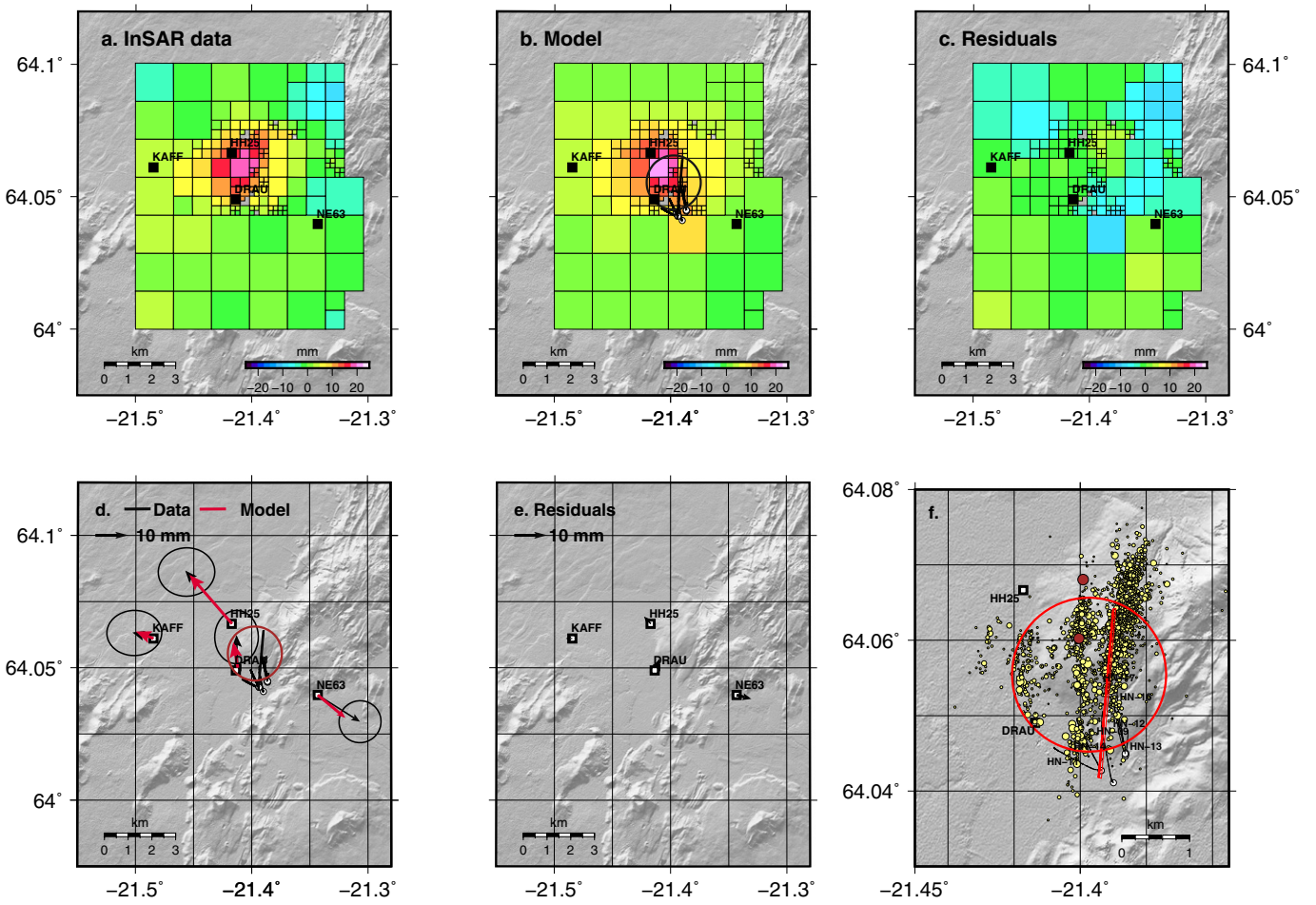

Fig. 7. Model B: Spherical pressure source and rectangular dislocation. InSAR data (a), model (b) and residuals (c) in the top row. All in LOS of the satellite. GPS data and model (d), residuals (e), as well as the location of the sources relative to the seismicity and the locations of the injection boreholes (f) in the bottom row. The rectangle marks the dislocation (bold line is the upper edge), the circle the spherical pressure source.

5.2. Fluid flow paths

In order to properly interpret the models, we need to consider the possible flow paths of the injected water. The injection was aimed at NE striking fractures that were supposed to lead the fluids towards the northwesternmost production boreholes at Hellisheidi, northeast of the injection site (north of HE-08, see Fig. 1). Tracer tests conducted 2013–2015 have confirmed that the injected water was partly recovered in the boreholes to the northeast, but not in holes southeast of the injection site (Kristjánsson et al., 2016). However, the total amount of recovered fluids range between 1% and 57% for the different injection holes (Kristjánsson et al., 2016). The recovery was estimated by sampling boreholes at the Hellisheidi power plant (Fig. 1), none of which are located directly north and northwest of the injection holes. This means that the amount of fluid flow to the north and northwest could not be determined. Khodayar et al. (2015) investigated possible structural flow paths in the Húsmúli area and found—in addition to the ENE striking fractures—northerly, WNW and NW striking, permeable fracture sets. These possible flow directions (North, NW and WNW) are required by Model B (see Section 4.2.2), while model A implies pressure build-up in direct vicinity of the injection site.

The end of the deformation transient in early 2012 indicates a change in the flow regime that caused the end of the pressure build-up. Most likely, this can be explained by two processes. The pressure increase N/NW/WNW of the injection site causes the pressure gradient to diminish, which results in reduced flow towards N/NW/WNW (only applies to model B). And, an increase in permeability towards other directions, caused by the induced seismicity could explain the observations.

Table 3
Parameters and 90% confidence intervals for model B after joint inversion of GPS and InSAR data. The shear modulus we use is $\mu = 10$ GPa and Poisson's ratio is $\nu = 0.25$.

Model B		
Free model parameters		13
No. of data		179
χ^2		157
Pressurized sphere		**90% CI**
Longitude [° W]	21.397	(21.380; 21.410)
Latitude [° N]	64.055	(64.048; 64.063)
Depth to center [km]	2.7	(2.2; 3.0)
ΔP [MPa]	1.0	(0.5; 2.0)
Radius [km]	1.1	(0.8; 1.4)
Dislocation		**90% CI**
Longitude [° W]	21.392	(21.388; 21.395)
Latitude [° N]	64.053	(64.051; 64.055)
Length [km]	2.5	(2.1; 3.0)
Width [km]	0.4	(0.2; 0.6)
Depth to top [km]	0.7	(0.5; 1.2)
Dip angle [°]	84	(76; 89)
RL-Strike-slip [m]	0.45	(0.24; 0.80)
Normal slip [m]	0.04	(0.01; 0.11)

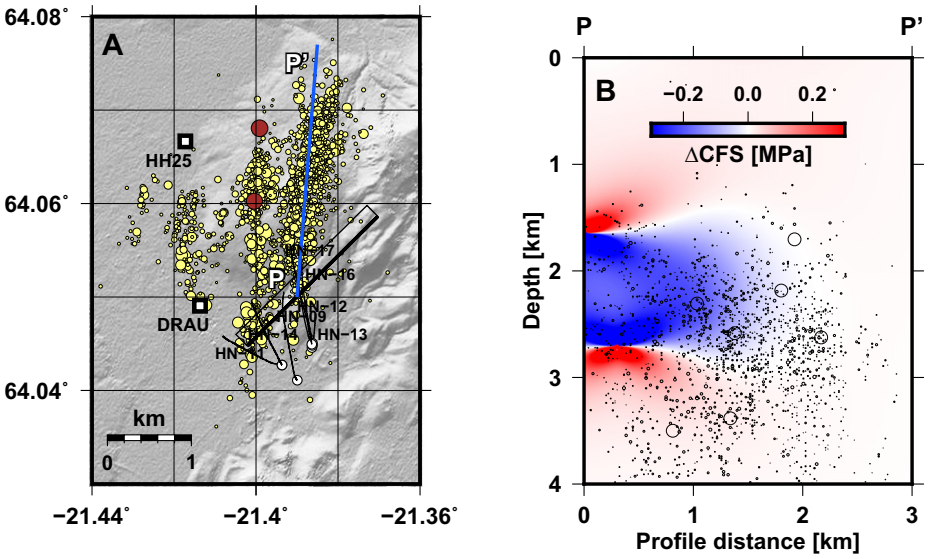

Fig. 8. Coulomb failure stress change calculated for model A. Plot A shows the location of the deformation source (black rectangle) and the profile (P-P′, blue line) on which ΔCFS is calculated. Yellow circles indicate earthquake locations (relocated from the SIL network), red circles indicate the M4 mainshocks of 15 October 2011. Plot B shows the ΔCFS profile, where warm (red) colors indicate an increase in Coulomb failure stress, cold (blue) colors a decrease. Black circles depict earthquake locations within 200 m of the P-P′ profile.

5.3. Model A

We interpret Model A as a steeply dipping opening fracture that is fed by the injection and is opening due to pressure increase (see Section 4.2.1). The location of the source is close to the injection site and the northeastern strike agrees with the main fracture orientation in the Hengill area. Hence, Model A offers a possible link between fluid injection and deformation (Fig. 6). The opening of a NE-SW trending crack is not outlined by the seismicity (Fig. 6), but could have occurred aseismically. An analogy to this might be aseismic magmatic dyke opening (see Ágústsdóttir et al., 2016). This model does not include deformation due to pore pressure increase in the seismically active area, hence the induced seismicity is either caused by a small increase in pore pressure that does not produce detectable surface deformation, or due to an increase in Coulomb failure stress.

We present a slightly altered version of this model in Supplement 2.1 (model S1), where we allow fault slip in addition to opening. Model A is more plausible because model S1 includes significant fault slip while not being aligned with the trend of seismic events. Hence, model A requires only aseismic opening whereas model S1 requires aseismic opening, strike-slip and dip-slip.

5.3.1. Stress changes

Changes in the stress field can bring faults closer to rupture and are a possible cause for induced seismicity (Harris, 1998; Segall and Lu, 2015). Whether or not a fault will fail due to stress changes depends on the change in Coulomb failure stress (ΔCFS, Beeler et al., 2000),

$$\Delta CFS = \Delta\tau_s + f\,(\Delta\sigma_n + \Delta p) \quad (2)$$

where $\Delta\tau_s$ is the change of shear stress in the slip direction, f is the coefficient of friction (which we set to 0.6 following Árnadóttir et al., 2003), $\Delta\sigma_n$ is the change in normal stress (tensile stress is positive) and Δp is the change in pore pressure.

We calculate static stress changes for Model A and estimate the change in Coulomb failure stress. We assume a receiver fault location in the easternmost zone at Húsmúli (which is the zone of initial seismic activity), with orientation according to the majority of focal mechanisms in this zone (strike of 5°, dip towards east of 75° and rake of −150°; i.e. right-lateral strike-slip with normal slip component).

As can be seen Fig. 8, we find that the majority of earthquakes (occurring at depths between 1.5 an 2.5 km)—and in particular the larger events—experience no change or a reduction in Coulomb failure stress (i.e. moving the receiver faults away from failure). We see no correlation between earthquake locations and changes in Coulomb failure stress and conclude that Model A is an unlikely explanation for the seismicity.

5.4. Model B

We interpret the spherical pressure source in Model B as an area of increased pore pressure (see Section 4.2.2). The center of the pressure source is located around 1 km north of the injection site which could indicate flow towards the north and northwest while flow from the injection site to the southeast is inhibited. From studies of flow paths (Kristjánsson et al., 2016) and structural geology (Khodayar et al., 2015) at Húsmúli (see Section 5.2), this seems quite possible. The pressure source covers much of the volume around the induced micro-seismicity, with the depth range of the source (depth to the center 2 to 3 km) agreeing very well with the depth of the earthquakes. This model therefore offers a plausible explanation for the seismicity, which would mean that seismogenic faults were pushed towards failure by increase of pore pressure. The pressure increase of 1.0 MPa estimated in this model is poorly constrained by the inversion (90% CI: 0.5 to 2.0 MPa) and can only be interpreted as an average bulk pressure increase in the area. In reality it is more likely that the pressure increase is most prominent close to the permeable N/WNW/NW fractures and in layers that are fed by those fractures.

The location of the dislocation model was not constrained for the inversion but agrees with the easternmost zone of micro-seismicity in Húsmúli. The fault model, however, does not coincide with the location of the two largest events—which presumably caused most of the co-seismic slip—further west. We tested a model of the surface displacements that would be caused by the two M4 events (Supplement 2.3) and found insignificant deformation. We also tested a model that combines pressure increase and two slipping faults with locations constrained to the zones of most seismicity (Supplement 2.4, Model S4). This model does not fit the data as well as either Model A or Model B.

It should be noted however, that the depth of the slipping part of the fault in Model B, extending from 0.7 to 1.1 km, is shallow compared to the seismicity which mostly occurred between 1.5 and 4.5 km. The seismicity depth, however, is sensitive to the velocity model that was used.

We can estimate the geodetic moment of the fault slip as $M_0 = \mu A u$ (where μ is the shear modulus, A is the fault surface area and u is the amount of slip), and find a value of 4.5×10^{15} N m (which corresponds to a seismic event of magnitude $M = 4.4$, related to M_0 through $M = 2/3 \log M_0 - 6.03$). This is one order of magnitude higher than the cumulative seismic moment released by the earthquakes in the easternmost zone of 0.4×10^{15} N m, based on relocated earthquakes detected by the SIL network. That would indicate that the slip that causes surface deformation is—at least in part—shallow, aseismic slip above the easternmost seismic zone in Húsmúli. This value of the geodetic moment, however, is strongly dependent on the shear modulus. While the value of 10 GPa that we use in our models is not an uncommon assumption (see Fialko and Simons, 2000; Juncu et al., 2017; Keiding et al., 2010), some studies indicate that values of shear modulus may be lower by up one to three orders of magnitude, especially in volcanic areas (e.g. Davis, 1986; Elsworth et al., 2008; Hutnak et al., 2009; Bromley et al., 2013). We test the effect of varying the shear modulus on the inversion results and present the results for $\mu = 1$ GPa in Supplement 2.5. Using this value results in a geodetic moment of 0.3×10^{15} N m, in good agreement with the seismic moment released by the earthquakes. This would indicate that the fault slip inferred from geodetic observations could be linked to the observed seismicity.

Instead of using a spherical pressure source, the pressure increase can be modeled using the pressurized horizontal circular crack model (Fialko et al., 2001), simulating a horizontal aquifer. The result is shown in Supplement 2.6 and very similar to that of Model B. Both models fall short of accurately simulating the complex three-dimensional reservoir geometry. We think, however, that the spherical source is a better representation because it implies that pressure change has a vertical extent which could represent multiple layers of fluid-storing rock formations, rather than a single layer.

5.4.1. Thermal expansion as a possible cause of deformation

Temperature, like pressure, can play a role in deformation in geothermal areas. If the injected fluid is warmer than the rock, thermal expansion can cause deformation (case a), or if (case b), in contrast, water is injected into rock that has a higher temperature, the water can boil and subsequent pressure increase can cause deformation (Hutnak et al., 2009). For case a, the rock must be colder than the water which has a temperature of 80 °C. For case b, water temperature needs to be above its boiling point which is approximately between 280 and 350 °C for depths between 1 and 3 km. While there are no temperature measurements available for the area affected by uplift at Húsmúli, we can look at the temperature distribution in and around the Hellisheidi reservoir (see Supplement 4 and Gunnarsson et al., 2011). The temperature in nearby boreholes is between 200 and 250 °C at 1000 m depth, at a distance of around 1–2 km away from the deforming area. Since we are interested in the area that is slightly outside of the central region of the reservoir we assume that it is unlikely for the temperature in the deforming area to be warmer than 250 °C, i.e. it is unlikely that is hot enough to satisfy case b — greater than 280 °C. At the same time, there are no observations of temperatures below 100 °C in the area (including observations in the peripheral region) which means that it is unlikely that temperatures at Húsmúli are cold enough to satisfy case a, i.e. less than 80 °C. We conclude that it is improbable that thermal effects contribute to the expansive deformation at Húsmúli. That said, the injected fluid is likely to be cooler than the rock formation and may cause contraction of the rock, opposing the pore-pressure driven expansion. Any thermal effect is therefore more likely to reduce the deformation signal, rather than enhance it.

5.4.2. Volumetric expansion compared to volume of injected water

We can compare the volume of injected water to the volumetric expansion of the rock formation to test whether or not the injection can plausibly be linked to the deformation. The expansion of the spherical pressure source in model B is around 4.2×10^5 m^3, given by the relation

$$\Delta V_r = \pi \Delta P a^3 / \mu \tag{3}$$

(Segall, 2010) and the parameters given in Table 3. The total volume of injected water between September 2011 and May 2012 is around $\Delta V_f \approx 13 \times 10^6$ m^3 (see Section 2). This implies a volume ratio of $\Delta V_f / \Delta V_r \approx 30$.

The volume change of the rock V_r is related to the volume of injected fluid V_f, and the relation depends on several material parameters (porosity ϕ, Poisson's ratio ν, Biot's coefficient α, bulk modulus of the rock formation K and bulk modulus of the fluid K_f), as described in Juncu (2018):

$$\frac{\Delta V_f}{\Delta V_r} = \frac{1}{f_e}\left[\alpha + \frac{3\phi}{\alpha}\frac{1-\nu}{1+\nu}\left(\alpha - 1 + \frac{K}{K_f}\right)\right]. \tag{4}$$

The factor f_e (with $0 \le f_e \le 1$) describes the effective fraction of the injected water that contributes to the deformation. It is 1 if all the injected water contributes to the deformation; it is less than 1 if some fraction is diverted to another area where it does not cause observable deformation, e.g. because it flows into the reservoir where fluid is being extracted, or because locally higher rock strength (i.e. higher shear/bulk modulus) results in negligible surface deformation.

Eq. (4) indicates that fluid compressibility is an important factor when interpreting the volume change of fluid bearing rock formations (see Juncu, 2018). This has also been observed in a volcanic setting when comparing calculated subsurface volume change to lava flow volumes (Johnson, 1987), as well as for models of volume changes during magma transfer between magma chambers and dykes (Rivalta and Segall, 2008).

Eq. (4) allows us to predict the volume ratio $\Delta V_f / \Delta V_r$ based on material parameters. The bulk modulus of water at 80 °C at pressures between 1 and 10 MPa is $K_f = 2$ GPa (Wagner and Kretzschmar, 2007). The assumed rock's shear modulus of $\mu = 10$ GPa and Poisson's ratio of $\nu = 0.25$ imply a bulk modulus of $K = 17$ GPa (related to μ and ν through $K = 2\mu(1+\nu)/(3(1-2\nu))$). The average recovery from the injection wells in the Hellisheidi reservoir is likely below 50% (see Section 5.2). If we assume that all injected water that is not flowing back into the reservoir is contributing to the deformation, this would mean that $f_e > 0.5$ in the Húsmúli area. As a limiting case we will test $f_e = 0.5$. Using likely values for porosity, $0.05 \le \phi \le 0.2$, and Biot's coefficient, $0.5 \le \alpha \le 1$, (see e.g. Juncu, 2018), we find that the maximum possible value we can reach with this parameter combination is $\Delta V_f / \Delta V_r \approx 10$, about one third of the observed volume ratio (see above).

In order to bridge the gap between the observed and the calculated volume ratios we have to revisit the assumptions that we made and consider unmodeled processes that might affect the deformation. We suggest that the following factors may influence the difference between observation and calculations:

- the value of the bulk modulus K. $\Delta V_f/\Delta V_r = 30$ can be reached with $K \approx 45$ GPa, when all other parameters remain unchanged.
- a porosity of $\phi > 0.2$, although changing the porosity alone would not suffice.
- a lower value for f_e (i.e. a smaller fraction of the injected water contributes to the deformation), of around $f_e = 0.15$ with all other parameters unchanged. This requires that a significant amount of the injected water (>30%) flows neither into the reservoir nor contributes to the deformation.
- if the injected water (80 °C) is colder than the surrounding rock (which is likely, see Section 5.4.1), contraction of the rock may occur, counteracting the expansion due to pore pressure increase.

As discussed in the beginning of Section 5.4, we think that the values for rock strength that we use in this study are already at the upper end of the possible spectrum, i.e. we assume that it is unlikely that $K > 17$ GPa. The porosity of geothermal reservoirs in Iceland is commonly assumed to be around 10% (see e.g. Axelsson et al., 2015). Hence, we think that $\phi > 0.2$ is unlikely. A low value of f_e is possible, but if we consider that only a limited amount of fluid flows back into the reservoir we are left with the question what happens to the portion of the injected liquid that is neither returned to the reservoir nor causes observable deformation. It is possible, however, that water flows to greater depths where rock strengths are higher, or that it diffuses over greater volume so that the pore pressure increase becomes small. The contraction effect of cooling is a realistic possibility, because cooling related to fluid injection in geothermal reservoirs is a common effect (e.g. at the Geysers geothermal field, USA, see Rutqvist and Oldenburg, 2008). Additional modeling, however, is required to test this hypothesis.

6. Conclusion

Using GPS and InSAR data we find approximately 2 cm of surface displacement occurring during the initial phase of reinjection of waste water at the Hellisheidi power plant. We explore a range of various models to explain the surface deformation and present two in this paper, of which model B is our preferred model. Model B is composed of two deformation sources, a spherical source of expansion and a rectangular dislocation with uniform slip. We argue that it is unlikely that the expansion is caused by thermal effects (Section 5.4.1). We suggest that a local in increase pore-pressure is the cause of the expansion. It is possible, however, that thermal contraction counter-acts the expansion due to pore-pressure increase, thus reducing its effect (see Section 5.4.2). We interpret our preferred model (Model B) as the combination of two different processes: an increase in pore pressure, and fault slip in the easternmost zone of induced seismicity. The model implies northward and north-westward flow from the injection site along permeable fractures resulting in pore pressure increase in adjacent formations. The induced pressure change causes surface deformation and increases the effective tensile normal stress on the active faults at Húsmúli. Hence, we assume that the induced seismicity and the fault slip that causes part of the surface deformation are a result of the increased pore pressure. We can not conclusively say whether or not the fault slip is directly linked to some of the micro-seismicity or if it is aseismic. The deformation transient ends when the flow regime changes, either due to permeability increase caused by the seismicity or due to a change in the pressure field caused by the pore pressure increase. Both the continuation of seismic swarms and the lack of subsidence after the deformation transient ended indicate that the pore pressure level remains elevated.

Acknowledgements

The authors would like to thank: Einar Gunnlaugsson from Reykjavik Energy (RE) for providing injection data from Hellisheidi; Bjarni Reyr Kristjánsson (RE) for discussions and advice regarding the geothermal power plant operations and tracer tests; Sarah Minson (U.S. Geological Service) for help with CATMIP and letting us use her code; Elías Rafn Heimisson (Stanford University, USA) for advice regarding Coulomb failure stress calculations; David Bekaert (University of Leeds, UK) for helpful advice on the InSAR processing; Sigurjón Jónsson (King Abdullah University of Science and Technology, KSA) for commenting on the manuscript and for providing his Quadtree code; Ólafur Flóvenz (ÍSOR) for comments on the manuscript; the crustal deformation group at IES for help with the GPS measurements in Hengill and discussions on the work in progress. For computing the elastic half-space models we use *DMODELS* (Battaglia et al., 2013). We would like to thank Philippe Jousset as well as two anonymous reviewers for their thorough review which helped us improve the manuscript. Many of the figures were prepared using the GMT software (Wessel and Smith, 1991; Wessel et al., 2013). The intermediate TanDEM-X digital elevation model used in the InSAR processing was provided by DLR under project IDEM_GEOL0123. COMET is the NERC Centre for the Observation and Modelling of Earthquakes, Volcanoes and Tectonics. This work was supported in part by grants from the Iceland Research Fund (grant numbers 130371-051/052/053 and174377-051) and the University of Iceland Research Fund (grant number HI-6489).

Appendix A. Supplementary data

Supplementary data to this article can be found online at https://doi.org/10.1016/j.jvolgeores.2018.03.019.

References

Ágústsdóttir, T., Woods, J., Greenfield, T., Green, R.G., White, R.S., Winder, T., Brandsdóttir, B., Steinthórsson, S., Soosalu, H., 2016. Strike-slip faulting during the 2014 Bárðarbunga-Holuhraun dike intrusion, central Iceland. Geophys. Res. Lett. 43, 1495–1503.

Ágústsson, K., Kristjánsdóttir, S., Flóvenz, Ó.G., Gudmundsson, O., 2015. Induced Seismic Activity during Drilling of Injection Wells at the Hellisheiði Power Plant, SW Iceland. Proceedings World Geothermal Congress 2015, Melbourne, Australia, 19–25 April 2015.

Altamimi, Z., Metivier, I., Collileux, X., 2012. ITRF2008 plate motion model. J. Geophys. Res. 117,

Árnadóttir, T., Hreinsdóttir, S., Gudmundsson, G., Einarsson, P., Heinert, M., Völksen, C., 2001. Crustal deformation measured by GPS in the South Iceland Seismic Zone due to two large earthquakes in June 2000. Geophys. Res. Lett 28 (21), 4031–4033.

Árnadóttir, T., Jónsson, S., Pedersen, R., Gudmundsson, G.B., 2003. Coulomb stress changes in the South Iceland Seismic Zone due to two large earthquakes in June 2000. Geophys. Res. Lett. 30 (5).

Árnadóttir, T., Lund, B., Jiang, W., Geirsson, H., Björnsson, H., Einarsson, P., Sigurdsson, T., 2009. Glacial rebound and plate spreading: results from the first countrywide GPS observations in Iceland. Geophys. J. Int. 177, 691–716.

Axelsson, G., Arnaldsson, A., Berthet, J.-C.C., Bromley, C.J., Gudnason, E.Á., Hreinsdóttir, S., Karlsdóttir, R., Magnússon, I.T., Michalczewska, K.L., Sigmundsson, F., et al. 2015. Renewability Assessment of the Reykjanes Geothermal System, SW-Iceland. Proc. of the World Geothermal Congress 2015.

Battaglia, M., Cervelli, C., Murray, J., 2013. Modeling crustal deformation near active faults and volcanic centers — a catalog of deformation models. U.S. Geological Survey Techniques and Methods. USGS., book 13, chap. B1, 96 p.

Beeler, N., Simpson, R., Hickman, S., Lockner, D., 2000. Pore fluid pressure, apparent friction, and Coulomb failure. J. Geophys. Res. Solid Earth 105, 25533–25542.

Bekaert, D.P.S., Hooper, A., Wright, T.J., 2015a. Reassessing the 2006 Guerrero slow-slip event, Mexico: implications for large earthquakes in the Guerrero Gap. J. Geophys. Res. Solid Earth 120, 1357–1375.

Bekaert, D.P.S., Walters, R.J., Wright, T.J., Hooper, A.J., Parker, D.J., 2015b. Statistical comparison of InSAR tropospheric correction techniques. Remote Sens. Environ. 170, 40–47.
Bessason, B., Ólafsson, E., Gunnarsson, G., Flovenz, O., Jakobsdóttir, S., Björnsson, S., Árnadóttir, T., 2012. Verklag vegna örvaðrar skjálftavirkni í jarðhitakerfum. Technical Report. Orkuveita Reykjavíkur, Reykjavik, Iceland.(In Icelandic).
Björnsson, G., 2004. Reservoir conditions at 3–6 km depth in the Hellisheidi geothermal field, SW-Iceland, estimated by deep drilling, cold water injection and seismic monitoring. Proceedings: Workshop on Geothermal Reservoir Engineering. Vol. 29. Stanford University, Stanford Geothermal Program, Stanford, California. pp. 26–28.
Böðvarsson, R., Rögnvaldsson, S.T., Slunga, R., Kjartansson, E., 1999. The SIL data acquisition system: at present and beyond year 2000. Phys. Earth Planet. Inter. 113, 89–101.
Böðvarsson, R., Rögnvaldsson, S.T., Jakobsdóttir, S.S., Slunga, R., Stefánsson, R., 1996. The SIL data acquisition and monitoring system. Seismol. Res. Lett. 67, 35–46.
Bromley, C., Brockbank, K., Glynn-Morris, T., Rosenberg, M., Pender, M., O'Sullivan, M., Currie, S., 2013. Geothermal subsidence study at Wairakei-Tauhara, New Zealand. Proc. Inst. Civ. Eng. Geotech. Eng. 166, 211–223.
Chopra, A.K., Chakrabarti, P., 1973. The Koyna earthquake and the damage to Koyna Dam. Bull. Seismol. Soc. Am. 63, 381–397.
Clifton, A.E., Sigmundsson, F., Feigl, K.L., Guðmundsson, G., Árnadóttir, T., 2002. Surface effects of faulting and deformation resulting from magma accumulation at the Hengill triple junction, SW Iceland, 1994–1998. J. Volcanol. Geotherm. Res. 115, 233–255.
Davis, P.M., 1986. Surface deformation due to inflation of an arbitrarily oriented triaxial ellipsoidal cavity in an elastic half-space, with reference to Kilauea Volcano, Hawaii. J. Geophys. Res. Solid Earth 91, 7429–7438.
Davis, S.D., Pennington, W.D., 1989. Induced seismic deformation in the Cogdell oil field of west Texas. Bull. Seismol. Soc. Am. 79, 1477–1495.
Decriem, J., Árnadóttir, T., Hooper, A., Geirsson, H., Sigmundsson, F., Keiding, M., Ófeigsson, B.G., Hreinsdóttir, S., Einarsson, P., LaFemina, P., Bennett, R.A., 2010. The 2008 May 29 earthquake doublet in SW Iceland. Geophys. J. Int. 181, 1128–1146.
Deichmann, N., Giardini, D., 2009. Earthquakes induced by the stimulation of an enhanced geothermal system below Basel (Switzerland). Seismol. Res. Lett. 80, 784–798.
Dorbath, L., Cuenot, N., Genter, A., Frogneux, M., 2009. Seismic response of the fractured and faulted granite of Soultz-sous-Forêts (France) to 5 km deep massive water injections. Geophys. J. Int. 177, 653–675.
Dzurisin, D., 2007. Volcano Deformation. Springer.
Einarsson, P., 1991. Earthquakes and present-day tectonism in Iceland. Tectonophysics 189, 261–279.
Einarsson, P., 2008. Plate boundaries, rifts and transforms in Iceland. Jökull 58, 35–58.
Ellsworth, W.L., 2013. Injection-induced earthquakes. Science 341, 1225942.
Elsworth, D., Mattioli, G., Taron, J., Voight, B., Herd, R., 2008. Implications of magma transfer between multiple reservoirs on eruption cycling. Science 322, 246–248.
Evans, K.F., Zappone, A., Kraft, T., Deichmann, N., Moia, F., 2012. A survey of the induced seismic responses to fluid injection in geothermal and CO_2 reservoirs in Europe. Geothermics 41, 30–54.
Feigl, K.L., Gasperi, J., Sigmundsson, F., Rigo, A., 2000. Crustal deformation near Hengill Volcano, Iceland 1993–1998: coupling between magmatic activity and faulting inferred from elastic modeling of satellite radar interferograms. J. Geophys. Res. 105, 655–25.
Fialko, Y., Khazan, Y., Simons, M., 2001. Deformation due to a pressurized horizontal circular crack in an elastic half-space, with applications to volcano geodesy. Geophys. J. Int. 146, 181–190.
Fialko, Y., Simons, M., 2000. Deformation and seismicity in the Coso geothermal area, Inyo County, California: observations and modeling using satellite radar interferometry. J. Geophys. Res. 105, 21,781–21,793.
Flóvenz, O.G., Ágústsson, K., Guðnason, E.Á., Kristjánsdóttir, S., 2015. Reinjection and Induced Seismicity in Geothermal Fields in Iceland. Proceedings World Geothermal Congress, Melbourne, Australia, 19–25 April 2015.
Gelman, A., Carlin, J.B., Stern, H.S., Dunson, D.B., Vehtari, A., Rubin, D.B., 2014. Bayesian Data Analysis. Third, CRC Press, Boca Raton, FL.
Gunnarsson, G., 2012. Niðurdæling í húsmúla - staða og horfur. Technical Report. Orkuveita Reykjavíkur (Reykjavik Energy)., (In Icelandic).
Gunnarsson, G., 2013a. Staða niðurdælingarmála. Technical Report. Orkuveita Reykjavíkur (Reykjavik Energy), Reykjavik, Iceland.(In Icelandic).
Gunnarsson, G., 2013b. Temperature Dependent Injectivity and Induced Seismicity-managing Reinjection in the Hellisheiði Field, SW-Iceland. GRC Transactions.
Gunnarsson, G., Arnaldsson, A., Oddsdóttir, A.L., 2011. Model simulations of the Hengill Area, southwestern Iceland. Transp. Porous Media 90, 3–22.
Gunnarsson, G., Kristjánsson, B.R., Gunnarsson, I., Júlíusson, B.M., 2015. Reinjection into a Fractured Reservoir-induced Seismicity and Other Challenges in Operating Reinjection Wells in the Hellisheidi Field, SW-Iceland. Proceedings World Geothermal Congress.
Gunnlaugsson, E., 2016. Hellisheiði - Vinnsluskýrsla 2015. Technical Report. Orkuveita Reykjavíkur (Reykjavik Energy), Reykjavik, Iceland.(In Icelandic).
Haraldsdóttir, S.H., 2014. Mælingareftirlit á vinnslusvæðum Hellisheiðarvirkjunar árið 2014. Technical Report 2014/052. ÍSOR, Reykjavik, Iceland.(In Icelandic).
Harris, R.A., 1998. Introduction to special section: stress triggers, stress shadows, and implications for seismic hazard. J. Geophys. Res. Solid Earth 103 (B10), 24347–24358.
Healy, J.H., Rubey, W.W., Griggs, D.T., Raleigh, C.B., 1968. The Denver Earthquakes. Science 161, 1301–1310.
Herring, T.A., King, R.W., Floyd, M.A., McClusky, S.C., 2015. Introduction to GAMIT/GLOBK, Release 10.6. Technical Report. Mass. Inst. Technol., Cambridge, MA, USA.
Hooper, A., 2008. A multi-temporal InSAR method incorporating both persistent scatterer and small baseline approaches. Geophys. Res. Lett. 35,
Hooper, A., Bekaert, D., Spaans, K., Arıkan, M., 2012. Recent advances in SAR interferometry time series analysis for measuring crustal deformation. Tectonophysics 514, 1–13.
Hreinsdóttir, S., Árnadóttir, T., Decriem, J., Geirsson, H., Tryggvason, A., Bennett, R.A., LaFemina, P., 2009. A complex earthquake sequence captured by the continuous GPS network in SW Iceland. Geophys. Res. Lett. 36,
Hutnak, M., Hurwitz, S., Ingebritsen, S.E., Hsieh, P.A., 2009. Numerical models of caldera deformation: effects of multiphase and multicomponent hydrothermal fluid flow. J. Geophys. Res. Solid Earth 114,
Jahr, T., Jentzsch, G., Gebauer, A., Lau, T., 2008. Deformation, seismicity, and fluids: results of the 2004/2005 water injection experiment at the KTB/Germany. J. Geophys. Res. Solid Earth 113,
Jakobsdóttir, S.S., 2008. Seismicity in Iceland: 1994–2007. Jökull 58, 75–100.
Johnson, D.J., 1987. Elastic and inelastic magma storage at Kilauea Volcano. US Geol. Surv. Prof. Pap. 1350, 1297–1306.
Jónsson, S., Zebker, H., Segall, P., Amelung, F., 2002. Fault slip distribution of the 1999 M_w 7.1 Hector Mine, California, earthquake, estimated from satellite radar and GPS measurements. Bull. Seismol. Soc. Am. 92, 1377–1389.
Juncu, D., 2018. Deformation of Geothermal Reservoirs: A Case Study in the Hengill Geothermal Area using Satellite Geodesy. University of Iceland.(Ph.D. thesis).
Juncu, D., Árnadóttir, T., Hooper, A., Gunnarsson, G., 2017. Anthropogenic and natural ground deformation in the Hengill geothermal area, Iceland. J. Geophys. Res. Solid Earth 122, 692–709.
Kampes, B.M., Hanssen, R.F., Perski, Z., 2003. Radar interferometry with public domain tools. Third International Workshop on ERS SAR Interferometry, 'FRINGE03'. Frascati, Italy.
Keiding, M., Árnadóttir, T., Jónsson, S., Decriem, J., Hooper, A., 2010. Plate boundary deformation and man-made subsidence around geothermal fields on the Reykjanes Peninsula, Iceland. J. Volcanol. Geotherm. Res. 194, 139–149.
Khodayar, M., Axelsson, G., Steingrímsson, B., 2015. Potential Structural Flow Paths for Tracers and Source Faults of Earthquakes at Húsmúli, Hengill, South Iceland. Technical Report 2015/035. ÍSOR.,
Kirkpatrick, S., Gelatt, C.D., Vecchi, M.P., 1983. Optimization by simulated annealing. Science 220, 671–680.
Kristjánsson, B.R., Axelsson, G., Gunnarsson, G., Gunnarsson, I., Óskarsson, F., 2016. Comprehensive tracer testing in the Hellisheidi Geothermal Field in SW-Iceland. Proceedings, 41st Workshop on Geothermal Reservoir Engineering.
Majer, E.L., Peterson, J.E., 2007. The impact of injection on seismicity at The Geysers, California Geothermal Field. Int. J. Rock Mech. Min. Sci. 44, 1079–1090.
McTigue, D.F., 1987. Elastic stress and deformation near a finite spherical magma body: resolution of the point source paradox. J. Geophys. Res. 92, 12,931–12,940.
Minson, S.E., Simons, M., Beck, J.L., 2013. Bayesian inversion for finite fault earthquake source models I — theory and algorithm. Geophys. J. Int. 194, 1701–1726.
Okada, Y., 1985. Surface deformation due to shear and tensile faults in a half-space. Bull. Seismol. Soc. Am. 75, 1135–1154.
Ottemöller, L., Nielsen, H., Atakan, K., Braunmiller, J., Havskov, J., 2005. The 7 May 2001 induced seismic event in the Ekofisk oil field, North Sea. J. Geophys. Res. Solid Earth 110,
Pedersen, R., Jónsson, S., Árnadóttir, T., Sigmundsson, F., Feigl, K.L., 2003. Fault slip distribution of two June 2000 M_w 6.5 earthquakes in South Iceland estimated from joint inversion of InSAR and GPS measurements. Earth Planet. Sci. Lett. 213, 487–502.
Rivalta, E., Segall, P., 2008. Magma compressibility and the missing source for some dike intrusions. Geophys. Res. Lett. 35,
Rögnvaldsson, S.T., Slunga, R., 1993. Routine fault plane solutions for local and regional networks: a test with synthetic data. Bull. Seismol. Soc. Am. 83, 1232–1247.
Rögnvaldsson, S.T., Slunga, R., 1994. Single and joint fault plane solutions for microearthquakes in South Iceland. Tectonophysics 237, 73–80.
Rutqvist, J., Oldenburg, C.M., 2008. Analysis of Injection-induced Micro-earthquakes in a Geothermal Steam Reservoir, The Geysers Geothermal Feld, California. Lawrence Berkeley National Laboratory.
Segall, P., 1989. Earthquakes triggered by fluid extraction. Geology 17, 942–946.
Segall, P., 2010. Earthquake and Volcano Deformation. Princeton University Press.
Segall, P., Lu, S., 2015. Injection-induced seismicity: poroelastic and earthquake nucleation effects. J. Geophys. Res. Solid Earth 120,
Shirzaei, M., Ellsworth, W.L., Tiampo, K.F., González, P.J., Manga, M., 2016. Surface uplift and time-dependent seismic hazard due to fluid injection in eastern Texas. Science 353, 1416–1419.
Sigmundsson, F., Einarsson, P., Røgnvaldsson, S.T., Foulger, G.R., Hodgkinson, K.M., Thorbergsson, G., 1997. The 1994–1995 seismicity and deformation at the Hengill triple junction, Iceland: triggering of earthquakes by minor magma injection in a zone of horizontal shear stress. J. Geophys. Res. 102, 15,151–15,161.
Slunga, R., 1981. Earthquake source mechanism determination by use of body-wave amplitudes — an application to Swedish earthquakes. Bull. Seismol. Soc. Am. 71, 25–35.
Slunga, R., Rögnvaldsson, S.T., Böðvarsson, R., 1995. Absolute and relative locations of similar events with application to microearthquakes in southern Iceland. Geophys. J. Int. 123, 409–419.
Stefánsson, R., Böðvarsson, R., Slunga, R., Einarsson, P., Jakobsdóttir, S., Bungum, H., Gregersen, S., Havskov, J., Hjelme, J., Korhonen, H., 1993. Earthquake prediction research in the South Iceland Seismic Zone and the SIL project. Bull. Seismol. Soc. Am. 83, 696–716.

Stefánsson, R., Halldórsson, P., 1988. Strain release and strain build-up in the South Iceland seismic zone. Tectonophysics 152, 267–276.
Vogfjörd, K., Nolet, G., Morgan, W., Allen, R., Slunga, R., Bergsson, B., Erlendsson, P., Foulger, G., Jakobsdóttir, S., Julian, B., et al. 2002. Crustal profiling in Iceland using earthquake source-arrays. AGU Fall Meeting Abstracts.
Vogfjörd, K., Slunga, R., 2003. Rupture in the South Iceland Seismic Zone forced by magmatic intrusion in the Hengill area. EGS-AGU-EUG Joint Assembly. vol. 1. pp. 9685.
Wagner, W., Kretzschmar, H.-J., 2007. International Steam Tables: Properties of Water and Steam based on the Industrial Formulation IAPWS-IF97. Springer Science & Business Media.
Wessel, P., Smith, W.H.F., 1991. Free software helps map and display data. Eos Trans. AGU 72, 445–446.
Wessel, P., Smith, W.H.F., Scharroo, R., Luis, J., Wobbe, F., 2013. Generic mapping tools: improved version released. Eos Trans. AGU 94, 409–410.
Zang, A., Oye, V., Jousset, P., Deichmann, N., Gritto, R., McGarr, A., Majer, E., Bruhn, D., 2014. Analysis of induced seismicity in geothermal reservoirs — an overview. Geothermics 52, 6–21.